



## Research Article

# CuInS<sub>2</sub> quantum-dot-modified g-C<sub>3</sub>N<sub>4</sub> S-scheme heterojunction photocatalyst for hydrogen production and tetracycline degradation

Jingjing Zhang<sup>a</sup>, Yue Zhao<sup>a</sup>, Kezhen Qi<sup>a,\*</sup>, Shu-yuan Liu<sup>b,\*</sup>

<sup>a</sup> College of Pharmacy, Dali University, Dali 671000, China

<sup>b</sup> Department of Pharmacology, Shenyang Medical College, Shenyang 110034, China

## ARTICLE INFO

## Article history:

Received 28 April 2023

Revised 19 June 2023

Accepted 20 June 2023

Available online 12 August 2023

## Keywords:

CuInS<sub>2</sub> QDs

g-C<sub>3</sub>N<sub>4</sub>

Photocatalysis

Hydrogen production

S-scheme heterojunction

## ABSTRACT

CuInS<sub>2</sub> quantum-dot (CIS QD)-modified g-C<sub>3</sub>N<sub>4</sub> (CN) catalysts (CIS/CN) were prepared with the aid of an in-situ growth process. The as-obtained photocatalysts were explored by measuring their crystallinity, surface morphology, binding energy and light absorption activity. The photocatalytic efficiency of the photocatalysts was evaluated through photocatalytic water splitting for hydrogen production and tetracycline (TC) antibiotic degradation under the simulated solar light and visible light respectively. The optimized sample (10CIS/CN) showed the best photocatalytic activity: producing 102.4 μmol g<sup>-1</sup> h<sup>-1</sup> of hydrogen in 1 h, or degrading 52.16% of TC in 120 min, which were respectively 48 or 3.4 times higher than the photocatalytic activity of CN itself. The enhancement in the efficiency of the composite system was principally accredited to the enlargement of light absorption, the more effective in charge transfer and the dropping of the charge carrier pair recombination through a formed S-scheme heterojunctional interface. This work is an effort to adjust CN-based polysulfide QD for speedy photocatalysis. The enriched photocatalytic activity grants a new sense for adjusting the optical properties of CN.

© 2023 Published by Elsevier Ltd on behalf of The editorial office of Journal of Materials Science & Technology.

## 1. Introduction

With the swift expansion of the world economy and societal progress, energy shortage and environmental problems have been developed as severe challenges in the present time [1]. For a long time, mining and refining nonrenewable fossil fuels are the main ways for human beings to obtain energy. However, during the use of hydrocarbon fuels, many pollutant gasses have been released, including CO<sub>2</sub>, SO<sub>x</sub> and NO<sub>x</sub>, which have posed a serious threat to animals, plants, people and the natural environment [2,3]. To improve the current energy consuming structure and meet the needs of social development, it is urgent to develop a green, competent and sustainable energy provider [4]. As one of the most superlative clean energy sources in the 21st century, hydrogen energy has an energy density that is 3 times that of gasoline, which has also other advantages including zero pollution, easy storage and recyclability, etc. Among many technologies, solar photocatalytic hydrogen production technology is considered as a sustainable, green and resourceful method [5]. Nature has provided high-quality con-

genital conditions in the form of abundant sunlight and plenty water resource to run hydrogen production technologies. However, as a core element, an appropriate catalyst determines the efficiency of photocatalytic reactions to the greatest extent, so as to transfer solar energy to hydrogen energy [6,7], CO<sub>2</sub> reduction [8,9] and pollutant degradation [10]. Therefore, synthesizing materials with a good visible light response and extraordinary photocatalytic activity is the key to realize such technologies.

It is known that, compared with TiO<sub>2</sub>, ZnO and other traditional UV-light-responsive photocatalysts, non-metallic g-C<sub>3</sub>N<sub>4</sub> (CN) has a good visible light response, together with a great ability to degrade pollutants and decompose water to generate hydrogen [11–16]. As a compound of the abundantly-available elements C and N, CN also has characteristics including a low cost, easy preparation, a high stability as well as a strong acid and alkali resistance [17]. However, it possesses some shortcomings and limitations. For example, the photogenerated charge carriers are easy to recombine because of its π-π-conjugated electronic structure limiting its own conductivity. Besides, a narrow visible light response (<460 nm), an insignificant specific surface and less active catalytic sites are responsible for the low photocatalytic activity of CN. To minimize the magnitude of these shortcomings, building a heterojunction is one of the effective ways to advance the photocatalytic talent of CN.

\* Corresponding authors.

E-mail addresses: [liushuyuan@symc.edu.cn](mailto:liushuyuan@symc.edu.cn) (S. Liu), [qkzh2003@aliyun.com](mailto:qkzh2003@aliyun.com) (K. Qi).

By combining two or more semiconductor materials through hydrothermal methods, in-situ growth methods, etc., the heterojunction material constructed has close interface contact, and its internal spatial potential difference may improve the separation rate of photogenerated charge carrier pairs, prolong the lifespan of photogenerated charge carrier pairs, and promote photocatalytic reactions [18]. In 2019, Yu et al. innovatively proposed the concept of S-scheme heterojunction [19]. S-scheme heterostructures are usually composed by n-type semiconductors, of which the work function of oxide is higher, the Fermi level is lower, and the work function of reductive is smaller, and the Fermi level is higher. In S-scheme heterojunctions, electrons migrate from reducing to oxidizing semiconductors, resulting in band bending of the energy band, internal electric field formation between interfaces, and accelerated charge transfer. At the same time, when the Fermi energy levels of the two photocatalysts are balanced, the energy band bending structure of the semiconductor surface makes the electrons and holes in the system recombine. Indeed, this process will eliminate the useless electrons and holes, and retain the strong reducing electrons on the CB of reductive and the strong oxidizing holes on the VB of oxide in the S-scheme heterojunction system to participate in the subsequent photocatalytic reaction. At present, there have been many literatures on g-C<sub>3</sub>N<sub>4</sub> based S-scheme heterojunctions, such as 0D/3D Bi<sub>3</sub>TaO<sub>7</sub>/g-C<sub>3</sub>N<sub>4</sub>, 1D/2D Bi<sub>2</sub>S<sub>3</sub>/g-C<sub>3</sub>N<sub>4</sub>, 2D/2D N-ZnO/g-C<sub>3</sub>N<sub>4</sub> and 3D/2D ZnO/g-C<sub>3</sub>N<sub>4</sub> [20–23].

As a zero-dimensional semiconductor nanomaterial, quantum dots (QDs) have many advantages, not possessing in one-dimensional and two-dimensional materials, such as huge surface area, prevalent visible light harvesting, a strong photoelectric conversion capability, multi exciton effect and quantum size effect [24]. Composites of QDs and CN can improve their shortcomings, for example, through the loading of QDs, the visible light absorption range of CN can be stretched to speed up the separation and migration rate of photogenerated charge carrier pairs [4]. In addition, through the loading of QDs, the number of reactive sites on the CN surface can be increased, the internal charge transfer paths can be shortened, and the photocatalytic performance can be effectively strengthened [25]. Relevant research has been conducted by many researchers including the deposition on CN by metal phosphide QDs [26], metal oxide QDs, metal sulfide QDs and carbon QDs [27]. In particular, the close interface contact provided by an inorganic polymeric heterostructure is conducive to the charge separation on the CN surface, which greatly promotes photocatalytic water decomposition to generate hydrogen [28].

In the field of photocatalysis, a direct narrow-band-gap CuInS<sub>2</sub> (CIS) material has captivated extra consideration due to its excellent solar energy conversion efficiency [29]. CIS has a direct band gap (1.50 eV) structure, with its light harvesting range extending to the near-infrared region. At the same time, it also has advantages including a high light absorption coefficient (~105 cm<sup>-1</sup> at 500 nm), a good stability and a low toxicity [30]. By composite with CN that has the conduction band (-1.30 eV) and the valence band (1.40 eV), CIS QDs are organically combined with CN in this work, so as to improve the photocatalytic activity by constructing a composite material system and applying it to the photocatalytic generation of hydrogen from water and to the degradation of TC antibiotic.

Here, CIS/CN photocatalysts have been synthesized through one-pot solvothermal method. The catalytic activity of the composites was inspected in combination with experiments of the photocatalytic hydrogen evolution through water splitting and the antibiotic oxidation. The photocatalytic efficiency of the CIS/CN composites was significantly better than that of CN. The expansion of the visible light harvesting activity and the discount in the photogenerated charge carrier recombination rate were main reasons for the excellent photocatalysis of CIS/CN composites. This

work is an attempt to modify CN with polysulfide QDs to enhance the activity of CN, which presents new solutions for designing high-performance heterojunctional photocatalysts.

## 2. Experimental section

### 2.1. Material

Copper nitrate, sodium hydroxide, sodium sulfate and barium sulfate were acquired from Sinopharm Chemical Reagent Co., Ltd. Urea was purchased from Tianjin Fengchuan Chemical Reagent Co., Ltd. Reduced glutathione, indium nitrate hydrate and tetracycline were purchased from McLean Reagent Co., Ltd. Sodium sulfide hydrate (Na<sub>2</sub>S·9H<sub>2</sub>O) was purchased from Nanjing Chemical Reagent Co., Ltd., and isopropanol was purchased from Xilong Scientific Reagent Co., Ltd.

### 2.2. Preparation

10 g of urea was grinded into fine powder and then heated in an aluminum oxide crucible at 520 °C for 240 min with the heating rate at 10 °C /min. Then, the samples were cooled in a muffle. The collected pale-yellow materials were grinded into fine powder to get CN particles.

About 0.1 mmol of Cu(NO<sub>3</sub>)<sub>2</sub>·3H<sub>2</sub>O, 0.8 mmol of InN<sub>3</sub>O<sub>9</sub>·xH<sub>2</sub>O and 2 mmol of L-Glutathione (GSH) were dissolved in 40 mL of deionized water. After ultrasonication for 10 min, NaOH solution (0.05 mol/L) was introduced dropwise while stirring for adjusting the pH of the solution to 8.5. The well-mixed homogenous mixture was shifted to a three-necked flask placed in a condensing device with the temperature elevated to 90 °C in a N<sub>2</sub> atmosphere. About 1.3 mmol of Na<sub>2</sub>S·9H<sub>2</sub>O in solution was quickly added for the chemical reaction at a constant temperature 90 °C for 60 min. The cooled precipitate was refined with isopropanol and deionized water, centrifuged and desiccated in vacuum at 25 °C. The brown product obtained was CuInS<sub>2</sub> QDs, which was labeled as CIS QDs.

To construct CIS/CN nanocomposites, different amounts of CuInS<sub>2</sub> (5, 8, 10, 12 and 15 wt.%) were mixed with a required amount of CN in an ethanol/water mixture to form a homogeneous paste, which was warmed to 80 °C while stirring to remove the liquid portion completely. The materials obtained were denoted as xCIS/CN, where 'x' refers to the percentage amount of CuInS<sub>2</sub> in the prepared nanocomposites.

### 2.3. Characterization

The crystal phase and purity of the samples were inspected using a Bruker X-ray powder diffractometer (XRD). The chemical bonds and functional groups of the photocatalysts were determined through Fourier infrared spectroscopy (FT-IR). The spectra were taken in a scanning range of 400–4000 cm<sup>-1</sup>. X-ray photoelectron spectroscopy (XPS) was handled to analyze the surface elemental composition and existing state of the photocatalysts. Transmission electron microscopy (TEM) and EDS tests were conducted to investigate the microstructure of the samples. TU-1901 ultraviolet visible absorption spectroscopy (UV vis DRS) was used to illustrate the optical absorption performance of the materials. BaSO<sub>4</sub> powder was used as a reference, with a scanning range of 200–800 nm. The photoluminescence spectrum was determined using a RF-5301 PC fluorescence spectrometer at an excitation wavelength of 325 nm.

### 2.4. Photocatalytic activity

A hydrogen production test was carried out in a photocatalytic system allied with a Shimadzu GC-14C gas chromatograph. The

light source was a 350 W Xe lamp allied with a 365 nm filter. The reaction mixture was composed of 80 mL of deionized water, 10 mL of triethanolamine (TEOA) and 20 mg of catalysts in a 100 mL three-necked glass flask to check the hydrogen production rate. Before reactions, the mixture was bubbled with N<sub>2</sub> for 30 min for deoxygenation. The amount of H<sub>2</sub> produced was checked after appropriate time.

The photocatalytic oxidation of tetracycline (TC) was comprehended with a 1 kW halogen lamp as the light source ( $\lambda > 420$  nm). 50 mg of sample was mixed with 100 mL (40 mg/L) of TC solution and stirred in dark for 30 min to adsorb TC units on the photocatalyst. The photocatalytic degradation test was extended to 120 min, and 5 mL of solution was separated every 20 min for the measurement of the degraded pollutants. After centrifugation, the sample was filtered to remove the photocatalyst, with an absorbance dignified to assess the decomposition of TC, which absorbs light in the range of 250–270 nm and 343–366 nm. For calculating the oxidation extent of TC, the reduction in peak intensity at 350–366 nm was monitored and selected as a reference.

### 2.5. Photoelectrochemical examination

Photoelectric characteristics including the flat band potential, transient photocurrent (*I-t*) and impedance spectroscopy (EIS) of CN, CIS QDs as well as 10CIS/CN were assessed. Experiments were carried out under an open-circuit-voltage mode through a three-electrode device in an electrochemical workstation (CHI660D). Wherein, Pt wires and saturated calomel electrodes were employed as the counters and reference electrodes respectively, with indium tin oxide glass (10 mm × 20 mm) coated with sample solution as a working electrode in 0.1 M Na<sub>2</sub>SO<sub>4</sub> electrolytic solution. Before investigation, nitrogen gas was effervesced through the solution for deoxygenation. When the open circuit potential was stable, the impedance potential method was employed to assess the flat band potential of the sample and the results were converted into a Mott Schottky curve. The photocurrent was also dignified in 0.1 M Na<sub>2</sub>SO<sub>4</sub> electrolyte solution. AC impedance spectroscopic measurement of the sample was conducted in the mixed solution of KCl and K<sub>3</sub>[Fe(CN)<sub>6</sub>]/K<sub>4</sub>[Fe(CN)<sub>6</sub>] at a scanning rate of 10 mV/s.

The preparation procedure of working electrodes is as follows: 16 mg of sample was disseminated in 3.6 mL of ethanol and 0.4 mL of 5% nafion solution. First of all, the photocatalysts were treated ultrasonically for 30 min followed by stirring for 4 h to form a homogeneous mixture. About 30  $\mu$ L of paste (4 mg/mL) was evenly employed on the conductive surface of ITO glass (10 mm × 10 mm) through doctor blade method. The samples prepared were kept silent for 1 h to avoid any disturbance, which were then desiccated with an infrared lamp to secure the working electrodes.

## 3. Results and discussion

### 3.1. Crystal structure analysis

The phase crystallinity of the photocatalysts was realized by taking their XRD spectra. Fig. 1(a) indicates the XRD pattern of CN, CIS QDs and CIS/CN. CN has two distinctive peaks at 13.1° and 27.5°, of which, the one at 13.1° belongs to the crystal plane (100) of CN formed by the repetition of the 3-s triazine structure on the plane, while the one at 27.5° is linked to the crystal plane (002) of CN, providing information about the interlayer stacking of the conjugated aromatic rings, which is a characteristic diffraction peak of graphite-like structures [31]. The diffraction peaks of CIS QDs at 28.0°, 46.5° and 55.2° corresponded to the crystal facets (112), (204) and (312) of the tetragonal CuInS<sub>2</sub> (JCPDS No.75–0106) system, indicating that the synthesized CIS nanocrystals possessed chalcopyrite structures [32]. The XRD pattern of CIS/CN and CN

was highly similar. It should be pointed out that the characteristic diffraction peak at 27.5° is the overlapping peak of crystal planes CIS (112) and CN (002). So, the crystal plane (002) of CN and (112) of CIS QDs were the main crystal planes exposed here. The more the amount of CIS QDs is loaded on CN, the broader and feebler the peak at 27.5° develops, reflecting that the loading of CIS QDs weakens the interlayer stacking effect of CN, and the peak at 13.1° also progressively faded away with the increase of CIS QDs. The peak at 46.5° is not obvious in the composite system, which is due to the small mass and poor crystallinity of CIS QDs in the samples.

The molecular structure and surface functional groups of the samples were analyzed using the FT-IR spectra provided in Fig. 1(b). Apparently, the spectra of CIS/CN composites with different proportions are similar to those of CN. The main characteristic diffraction peak at 810 cm<sup>-1</sup> originates from the stretching mode of the typical homotriazine heterocyclic conjugate structure in CN [33]. Peaks in the range of 1670–1220 cm<sup>-1</sup> are commanded under the stretching mode of C=N and C-N on the carbon nitrogen ring [34]. The wide peak at 3350–3020 cm<sup>-1</sup> is recognized to the stretching vibration of N-H and O-H bonds [35]. The above results show that CN still has a stable structure in the composite system. In addition, according to literatures, the FT-IR peaks of both CIS QDs and composites at 2340 cm<sup>-1</sup> are dominated by the stretching vibration of CO<sub>2</sub>, which might come in with the inadvertently-introduced air [36]. Because of its inorganic origin, the characteristic FT-IR peak of CIS QDs was weak and difficult to analyze. It is seen from the FT-IR spectra of the composites that the loading of CIS QDs slightly weakens the tensile vibration diffraction peak of the triazine ring structure in the CN conjugated system, but the system still retains a good CN heterocycle structure which in good agreement with the XRD data.

### 3.2. XPS

The bonding and chemical state of elements in 10CIS/CN were evaluated through XPS. Fig. 2(a) presents the XPS full spectrum of the 10CIS/CN sample, which contains all the constituent elements like C, N, Cu, In and S. A small amount of O was also detected, which might come from the adsorbed water. Fig. 2(b) presents the high-resolution XPS data of Cu 2p. The peaks at 952.1 and 932.3 eV belong to Cu 2p<sub>1/2</sub> and Cu 2p<sub>3/2</sub>. The split of orbit calculated between the two peaks is 19.8 eV, revealing that Cu is available in the composite as Cu<sup>+</sup> [37]. Fig. 2(c) shows the high-resolution spectra of In 3d. The XPS peak of In 3d<sub>3/2</sub> and In 3d<sub>5/2</sub> is respectively available at 452.1 and 444.8 eV, indicating that In exists as In<sup>3+</sup> [38]. The XPS peak fitting of S in Fig. 2(d) illustrates that the high-resolution spectra of S 2p involves two peaks at 164.0 and 162.0 eV due to the spin-orbit coupling interaction, and they are commanded by the In-S and Cu-S bonding structure respectively, indicating that S exists in the form of S<sup>2-</sup> [39,40]. Fig. 2(e) displays the XPS spectrum of C 1s, the peaks available at 288.2, 287.5 and 285.0 eV are ascribed to the N=C=N bond in the aromatic ring with sp<sup>2</sup> hybridization, N-CH bond on the edges of heptazine unit and sp<sup>2</sup> hybridized C-C bond, respectively. Fig. 2(f) shows the spectrum of N 1s. After XPS peak fitting, three peaks are visible at 401.0, 399.9 and 398.7 eV, which respectively correspond to C-NH, N-(C)<sub>3</sub> and C-N=C groups in the triazine ring structure [22]. The outcomes of XRD, TEM and XPS show that CIS/CN photocatalysts were successfully synthesized in this work.

### 3.3. TEM

The morphology and microstructure of 10CIS/CN photocatalysts were achieved by measuring the TEM image delivered in Fig. 3(a). CIS QDs are uniformly developed on the surface of CN, which is

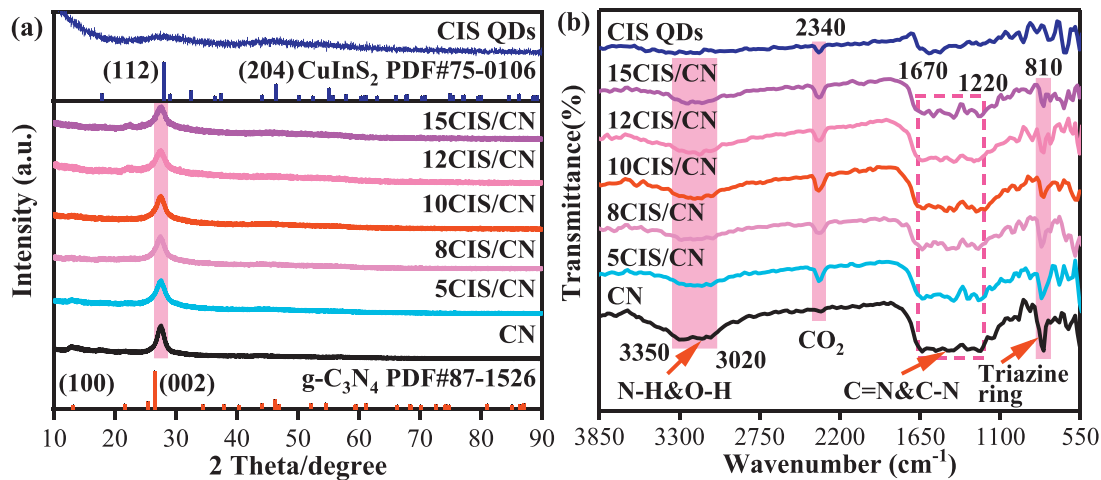


Fig. 1. XRD pattern (a) and FT-IR diagram (b) of CN, CIS QDs and CIS/CN.

composed of thin layers with folded and irregularly-folded structures, indicating that CIS QDs have a wider attachment area. The particle size of CIS QDs is about 5–8 nm, and that of CN is in a sheet structure. The HRTEM image in Fig. 3(b) shows that CIS QDs have highly-parallel and ordered lattice stripes, indicating that they have a high crystallinity with a lattice stripe spacing of 0.193 nm and 0.240 nm, which is consistent with the lattice spacing of crystal plane (204) and (211) of chalcopyrite type  $\text{CuInS}_2$  [41]. HRTEM images clearly show the deposition state of CIS QDs on the CN surface. Fig. 3(c) shows the elemental distribution map. The composite contains uniformly-dispersed elements like Cu, In, S, C and N, which shows that CIS QDs and CN have a good combination in the composite.

### 3.4. Energy band structure

The investigation of light absorption activity of the photocatalysts was achieved by measuring the UV-Vis DRS provided in Fig. 4(a). The absorption edge of CN is found near 441 nm, while CIS QDs has excellent optical absorption performance in a range of 300–750 nm [42]. Compared with CN, the photon harvesting activity of the composite materials in a range of 300–700 nm gradually increases with the increase of CIS QD content, indicating that the light absorption performance of CIS/CN is improved with the loading of CIS QDs. The enhancement of light absorption and photocatalytic activity may also be attributed to the strong electron coupling between CIS QDs and CN. The energy band structure of photocatalysts directly influences the redox reactions on their surface. Therefore, the Tauc formula (Eq. (1)) is used to convert the UV-vis absorption data to obtain the Kubelka Munk function diagram (Fig. 4b) [43], from which while the band gap value ( $E_g$ ) of the three samples CN, CIS QDs and 10CIS/CN can be determined by extrapolation method:

$$(\alpha h\nu)^n = A(h\nu - E_g) \quad (1)$$

where  $\alpha$ ,  $A$  and  $h\nu$  represent the absorption coefficient, proportional coefficient and photon energy,  $E_g$  refers to the band gap and  $n$  is a constant ( $n = 2$  denotes the direct transitions and  $n = 1/2$  indicates indirect transitions). In this work, CIS QDs is direct transition semiconductor, while CN is indirect transition semiconductor [44,45]. Therefore, the band gap energy of CN and CIS QDs is 2.81 eV and 1.92 eV, respectively, which agrees with the literature reports [46,47].

Fig. 4(c) represents the Mott-Schottky data of CN and CIS QDs. All the slopes are positive, indicating that the sample can be

judged as an n-type semiconductor [48]. The linear intercept of CN and CIS QDs on the x-axis is  $-0.53$  V and  $-0.90$  V (vs. SCE). The flat band potential ( $V_{fb}$ ) is calculated by Eq. (2), the corresponding  $V_{fb}$  of CN and CIS QDs is  $-0.56$  V and  $-0.93$  V, respectively.

$$V_0 = V_{fb} + \frac{RT}{F} \quad (2)$$

where  $V_0$  is the intercept of tangent line of Mott-Schottky curve and x-axis,  $R$  is the standard molar gas constant,  $T$  is the thermodynamic temperature, and  $F$  is the Faraday constant.

The conduction band potential ( $E_{CB}$ ) is calculated by Eq. (3), the  $E_{CB}$  of CN and CIS QDs is  $-0.66$  V and  $-1.03$  V (vs. SCE), respectively.

$$E_{CB} = V_{fb} - kT \ln \frac{N_c}{N} \quad (3)$$

where  $k$  is the Boltzmann constant,  $N_c$  is the effective density of states of the conduction band, and  $N$  is the doping concentration. In the approximate calculation, the value of  $kT \ln(N_c/N)$  is 0.1 eV.

The valence band potential ( $E_{VB}$ ) is then calculated by Eq. (4). As  $E_g$  values of CN and CIS QDs is 2.81 eV and 1.92 eV, respectively (Fig. 4(b)). The calculated  $E_{VB}$  of CN and CIS QDs is 2.15 V and 0.89 V, (vs SCE) respectively, as is illustrated in Fig. 4(d). As the loading amount of CIS increases, the color of CN samples gradually changes from light yellow to dark yellow (Fig. 4(e)).

$$E_{VB} = E_{CB} + E_g \quad (4)$$

### 3.5. Photoelectric performance

The steady-state PL spectrum is an effective method for analyzing the recombination of photogenerated charge carrier pairs in photocatalysts. As we know, the PL spectrum of materials is generated by the recombination of photo-generated charge carrier pairs within themselves. The stronger the emission peak intensity of the fluorescence spectrum, the higher the electron hole recombination rate inside the catalyst. Fig. 5(a) represents the steady-state PL spectrum. It can be seen that the fluorescence intensity of CIS/CN composites is far lower than that of CN, demonstrating that the loading of CIS QDs helps to retard the recombination rate of the excited charge pairs in CN and extending their lifetime. Thus, it also provides the system with more free electrons and holes to participate in the oxidation and reduction reactions between photocatalysts and reactants. In this system, the fluorescence intensity of 10CIS/CN is obviously decreased indicating that high amount of CIS has relatively strong inhibitory effect on the photogenerated

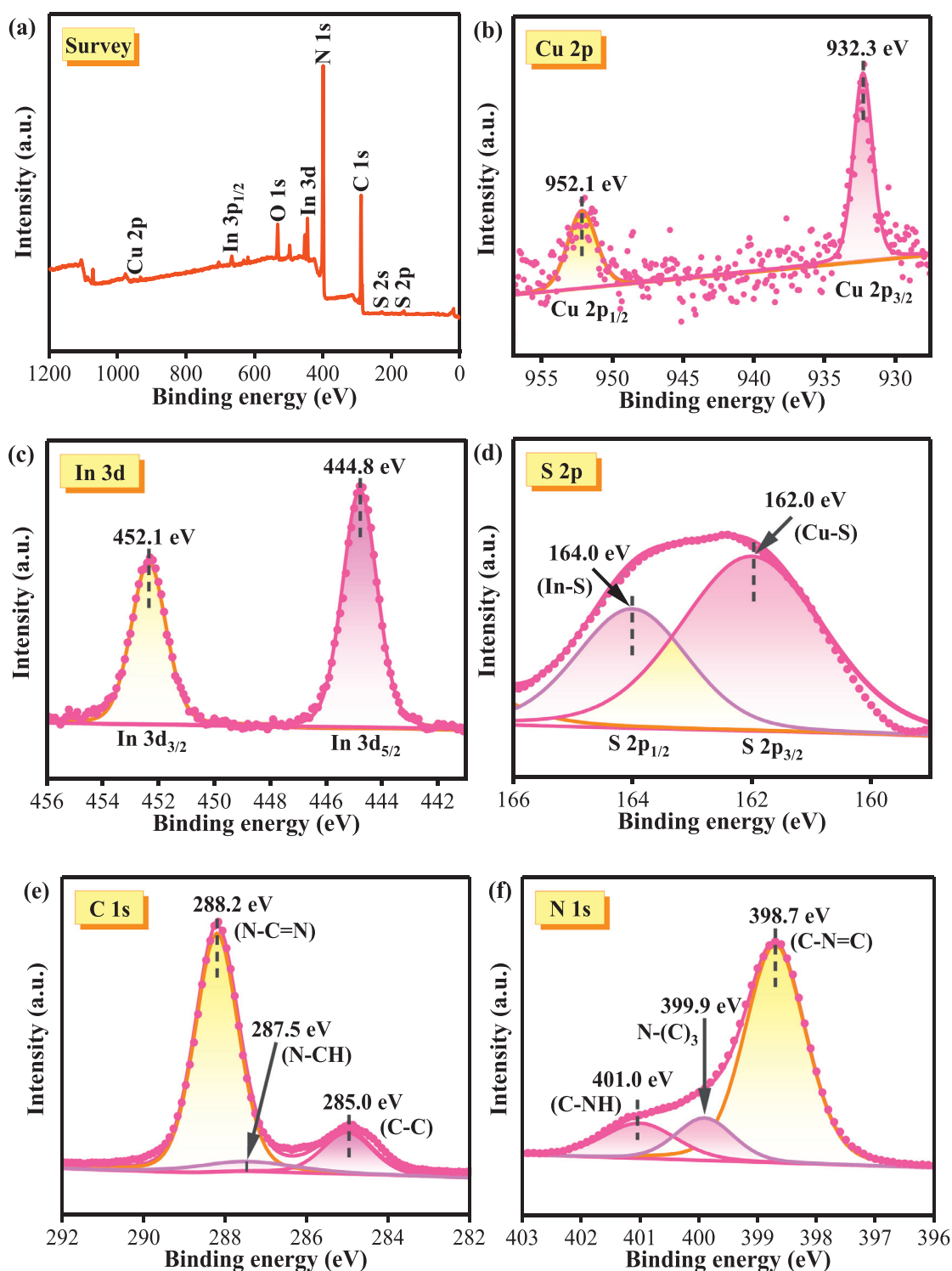


**Fig. 2.** XPS spectra of 10CIS/CN: survey XPS spectra (a) and high-resolution XPS spectra of Cu 2p (b), In 3d (c), S 2p (d), C 1s (e) and N 1s (f).

charge carrier recombination. The CIS QDs loading plays a special role in reducing the charge carrier pairs recombination rate of CN during the photocatalytic process, so it is one reason of the enhanced photocatalytic performance. As shown in Fig. 5(b), the data of transient fluorescence spectroscopy once again verify the extended photo-generated carrier lifetime of CIS/CN composite. Compared with CN (4.96 ns), the average PL life of 10CIS/CN (3.49 ns) is shorter, indicating that charge carrier pair separation is faster in composite.

Fig. 5(c) shows the transient photocurrent curves of the photocatalysts. The curve of 10CIS/CN ( $0.7233 \mu\text{A}/\text{cm}^2$ ) is significantly better than that of CN ( $0.2322 \mu\text{A}/\text{cm}^2$ ), revealing that the separation rate of  $e^-$  and  $h^+$  in the composite system is significantly enhanced. Besides, the EIS results are shown in Fig. 5(d). The half arc of the Nyquist curve of 10CIS/CN composite is smaller than that of CN, indicating that with the loading of CIS QDs, the interface charge transfer impedance of CN is reduced, resulting in accelerating of the charge transfer rate. From the photocurrent and

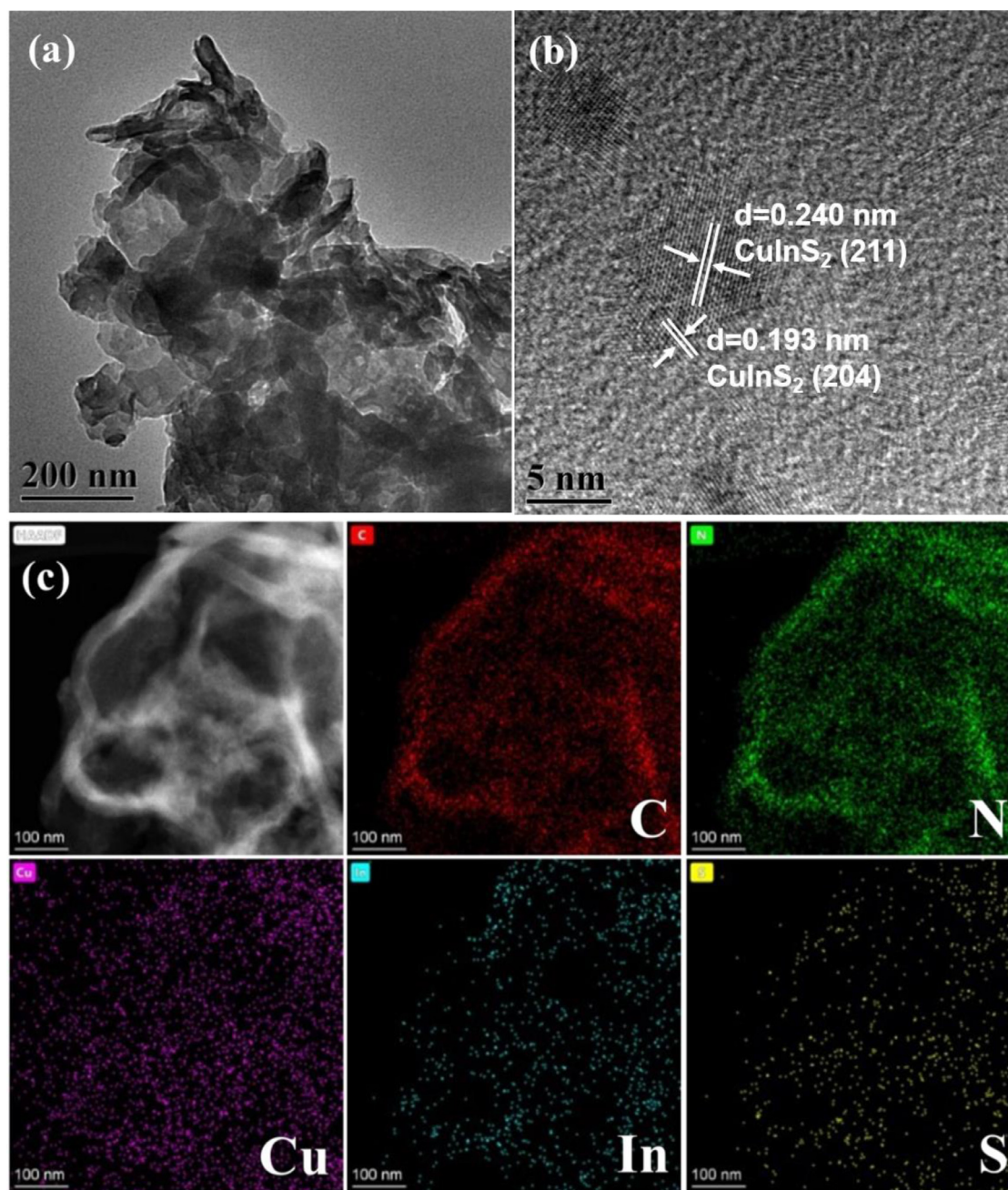


Fig. 3. (a) TEM, (b) HRTEM and (c) STEM-EDS elemental mapping of 10CIS/CN.

impedance spectra, it can be seen that through the loading of CIS QDs, the charge separation and transformation performance of CN is significantly enhanced.

In summary, the results from steady-state PL spectrum, transient fluorescence spectroscopy, transient photocurrent curves and EIS data, all indicate that the synergistic effect of intramolecular electric field and S-scheme heterojunction significantly accelerates the rapid transfer of photogenerated carriers within the materials and at the interface.

### 3.6. Photocatalytic activity

The catalytic behavior of the photocatalysts was firstly checked by separating hydrogen from water under the simulated solar light. As is provided in Fig. 6(a), all the CIS/CN composites show a better hydrogen evolution with a production rate that is superior

to that of CN. After combining with CIS QDs, the nanocomposite CIS/CN delivers a high hydrogen generation activity. With an increase in the loading amount of CIS QDs, the hydrogen evolution also steadily increases. For 10% CIS QDs, the quantity of hydrogen produced attains  $102.4 \mu\text{mol g}^{-1} \text{h}^{-1}$ . However, with a further increase in the loading amount of CIS QDs, the hydrogen evolution reduces obviously, for example, 12CIS/CN delivers  $85.2 \mu\text{mol g}^{-1} \text{h}^{-1}$  hydrogen, which may credit to the poor charge carrier pair separation and the competitive light absorption between CIS QDs and CN in 12CIS/CN, both of them reduce the capability of the photocatalysts to generate hydrogen. Compared this work with previous reports, the composite catalyst we prepared also showed high hydrogen evolution activity, as shown in Table 1.

We further evaluated the catalytic performance of the photocatalysts by degrading TC antibiotic, and the data is presented in Fig. 6(b) and (c). Irradiate under visible light for 120 min, the

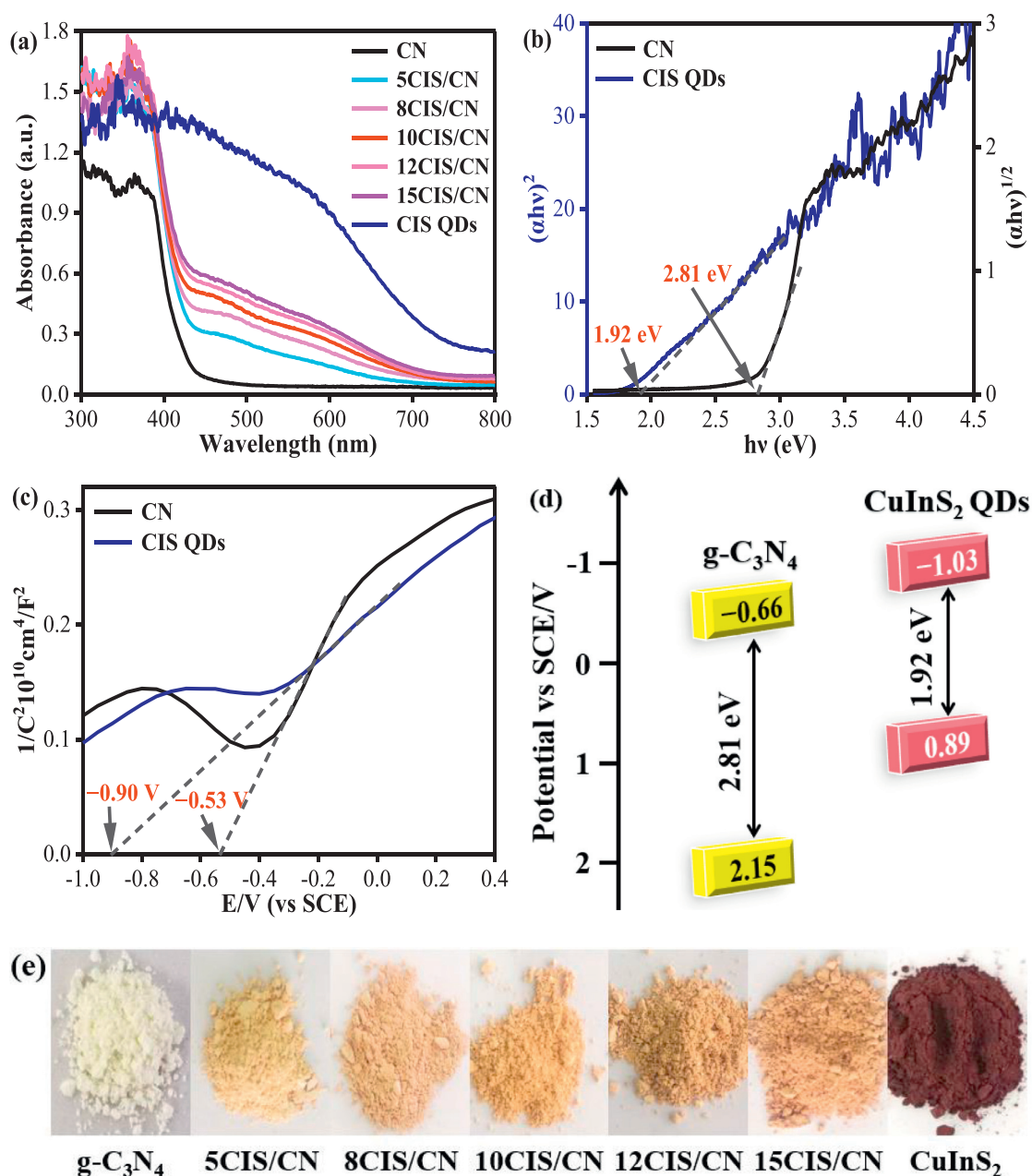


**Fig. 4.** Solid UV-vis absorption spectra (a), calculated band gap energy (b), Mott Schottky curve (c), the energy band structure (d) of CN and CIS QDs, and the photo pictures of the synthetic samples (e).

**Table 1**

Hydrogen evolution activity for 10CIS/CN in comparison with other reported CN-based catalysts.

Photocatalyst	H <sub>2</sub> evolution amount	Light source	Reference
Cu <sub>7.2</sub> S <sub>4</sub> /g-C <sub>3</sub> N <sub>4</sub>	82 μmol g <sup>-1</sup> h <sup>-1</sup>	NIR. (λ > 800 nm)	[49]
Ni(OH) <sub>2</sub> @g-C <sub>3</sub> N <sub>4</sub> /halloysite	18.42 μmol h <sup>-1</sup>	Vis. (λ > 400 nm)	[50]
3%Co <sub>3</sub> O <sub>4</sub> /g-C <sub>3</sub> N <sub>4</sub>	105.06 μmol g <sup>-1</sup> h <sup>-1</sup>	Simulated solar	[51]
TiC <sub>2</sub> /g-C <sub>3</sub> N <sub>4</sub>	47.5 μmol g <sup>-1</sup> h <sup>-1</sup>	Simulated solar	[52]
3%Ni <sub>2</sub> P/g-C <sub>3</sub> N <sub>4</sub>	128.7 μmol g <sup>-1</sup> h <sup>-1</sup>	300 W Xe lamp (λ > 420±10 nm)	[53]
10%CuInS <sub>2</sub> /g-C <sub>3</sub> N <sub>4</sub>	102.4 μmol g <sup>-1</sup> h <sup>-1</sup>	350 W Xe lamp (λ ≥ 365 nm)	This work

degradation rate of 50 mg of CN photocatalyst in 100 mL (40 mg/L) of TC solution is 15.31%. The photocatalytic activity is improved when both CIS QDs and CN are coupled to form nanocomposites. As the amount of CIS QDs increases in nanocomposites, the photocatalytic activity of the composites is gradually enhanced. Among them, 10CIS/CN shows decent activity, and the oxidation rate of TC

reached 52.16% after 120 min. For composites with a higher proportion of loading, the activity of 12CIS/CN and 15CIS/CN decrease slightly, which indicating that loading an appropriate amount of CIS is crucial for improving photocatalytic activity. In this work, 10CIS/CN is the best; lower CIS content will lead to insufficient surface redox active site, while higher CIS content may lead to com-

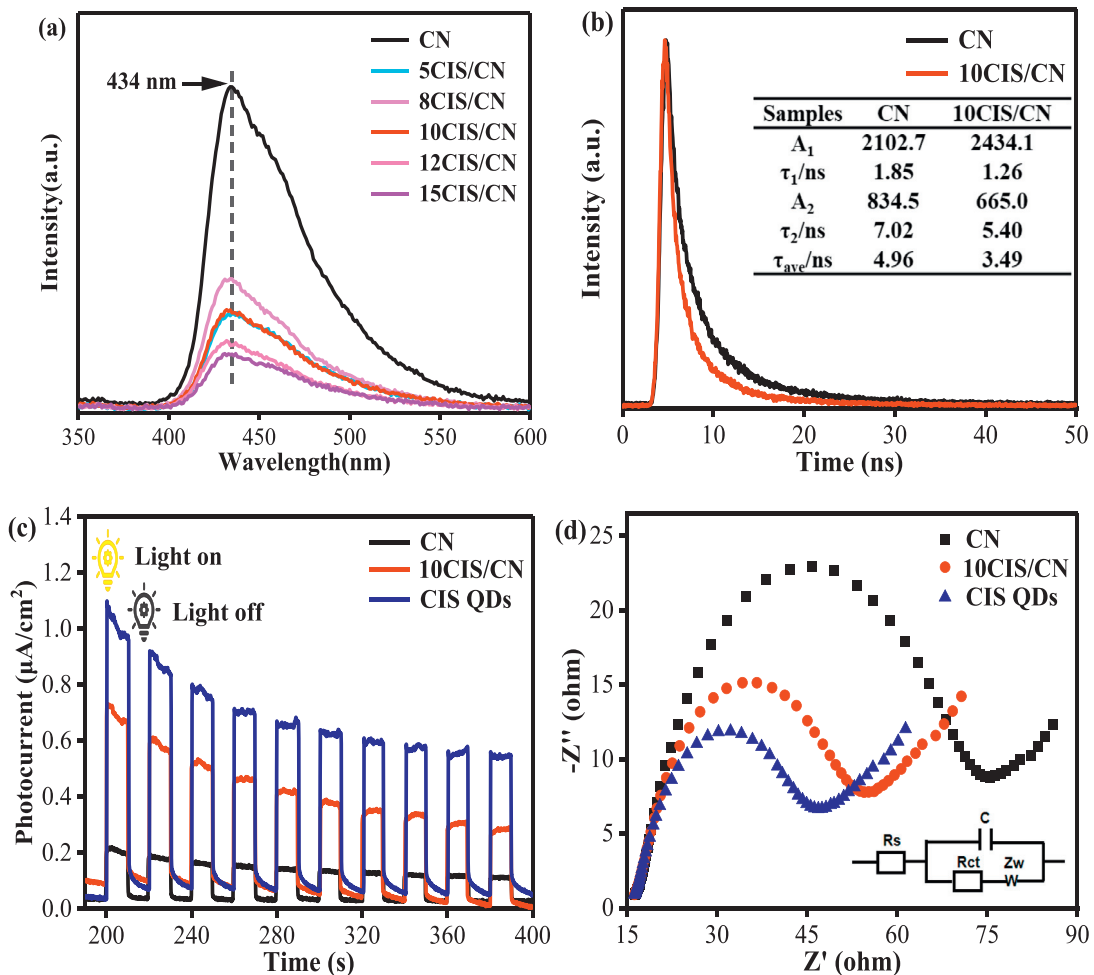


Fig. 5. Photoelectric property of CN, CIS QDs and 10CIS/CN: (a) steady PL spectra, (b) transient fluorescence spectra, (c) photocurrent response, (d) AC impedance spectrogram.

petitive light absorption between CIS and CN, both of which will lead to reduced activity of samples. The stability of the optimized sample (10CIS/CN) is shown in Fig. 6(d). Compared to unused sample, the XRD spectrum of 10CIS/CN does not change after the reaction of degrading of TC and producing H<sub>2</sub>, which further verifies the excellent stability of the 10CIS/CN photocatalyst.

### 3.7. Photocatalytic mechanism

To investigate the major degrading agents, the optimized 10CIS/CN composites were selected, followed by the same protocol mentioned in the photocatalytic degradation of tetracycline. During the process of photocatalysis, 1 mL of each of 0.01 mol/L benzoquinone (BQ), n-butanol (n-BA), disodium EDTA-2Na and potassium persulfate (KPS) solution was separately added to the reaction mixture before turning on the light source, in order to trap the superoxide radicals ( $\cdot\text{O}_2^-$ ), hydroxyl radicals ( $\cdot\text{OH}$ ), holes ( $h^+$ ) and electrons ( $e^-$ ), respectively. The data of radical/charge capturing experiments are collected using 10CIS/CN samples and presented in Fig. 7(a). The obtained results show that the oxidation rate of TC does not change significantly when n-BA or KPS is added, indicating that  $\cdot\text{OH}$  and  $e^-$  are not main active degrading agents. However, in the presence of BQ, the eradication rate of TC is greatly reduced, signifying that  $\cdot\text{O}_2^-$  is a main active agent responsible for the target redox reactions. The degradation rate in the presence of EDTA-2Na also shows that  $h^+$  participates in the photodegradation process of TC.

The presence of  $\cdot\text{O}_2^-$  and  $\cdot\text{OH}$  in the photocatalytic reaction is further detected by the electron spin resonance (ESR) spectra, with 5,5-Dimethyl-1-pyrroline N-oxide (DMPO) as the capture agent, and the results are shown in Fig. 7(b). Under dark conditions, no signal peaks were detected. After 10 min of light irradiation, four DMPO- $\cdot\text{O}_2^-$  characteristic signal peaks with a standard intensity of 1:1:1:1 and six weaker DMPO- $\cdot\text{OH}$  signal peaks were detected. This result is consistent with the results of the data of radical capturing experiments (Fig. 7(a)), once again proving that  $\cdot\text{O}_2^-$  is the main active species.

The work function is related to the Fermi level ( $E_f$ ) of the samples through the following equations:

$$W = W_{\text{tip}} + e\text{CPD}_{\text{sample}} \quad (5)$$

$$E_f = -W \quad (6)$$

where  $W$  and  $W_{\text{tip}}$  are the work function of the testing material and gold (4.25 eV),  $e$  is the charge on electrons, and  $\text{CPD}_{\text{sample}}$  is the contact potential difference (CPD) value obtained from the sample [54]. The  $e\text{CPD}_{\text{sample}}$  value of CN, CIS/CN and CIS is 0.27, 0.19 and 0.14 eV, respectively. Based on Eq. (5), the work function of CN, CIS/CN and CIS is 4.52, 4.44 and 4.39 eV respectively whose Fermi level are -4.52, -4.44 and -4.39 eV respectively according to Eq. (6). Based on the obtained results, it is obvious that when CIS and CN are combined to form composites, the electrons in the CB of CIS sink to CN and the process continues till the  $E_f$  level of both is equilibrated (Fig. 8(a)). Thus, CIS exhibits an upward band

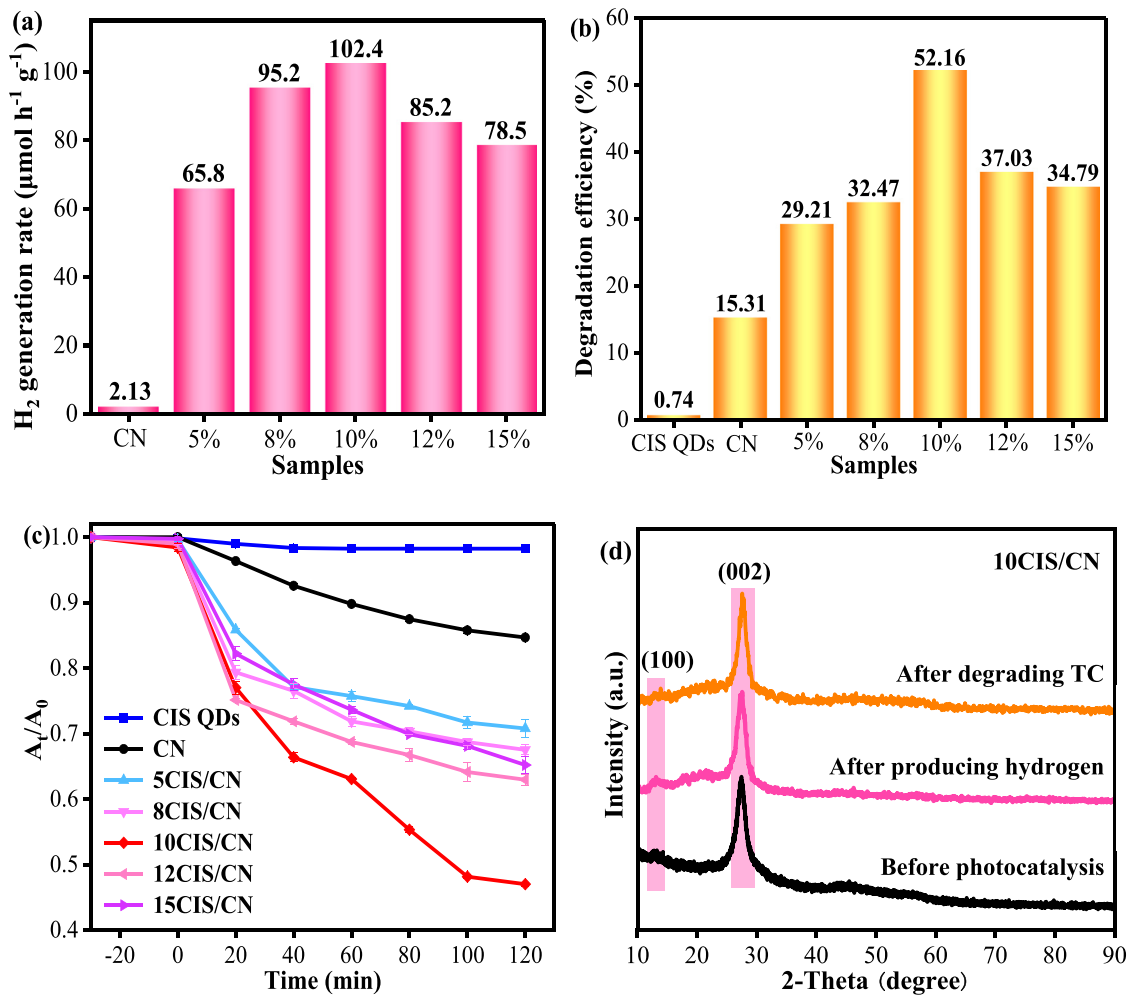


**Fig. 6.** (a) hydrogen generation rate, (b) TC degradation efficiency in 120 min and (c) TC degradation curve of CN and CIS/CN, (d) XRD patterns of 10CIS/CN before and after photocatalytic reaction.

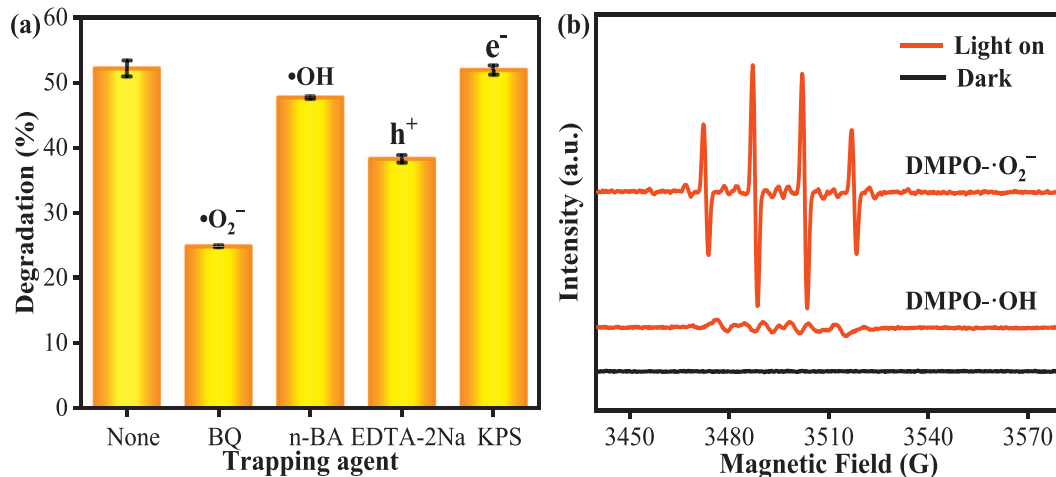


**Fig. 7.** (a) Photocatalytic degradation efficiency of TC over 10CIS/CN after adding active species capturing agents and (b) DMPO-•O<sub>2</sub><sup>-</sup> and DMPO-•OH of 10CIS/CN tested by DMPO spin-trapping ESR spectra.

bending at the interface due to its positive characters associated with the loss of electrons (Fig. 8(b)), while CN shows a downward band bending due to its negative characters associated with the gain of electrons. In consequence, the transfer of electrons creates an inner electric field (IEF) at the interface pointing from CIS to CN. When CIS/CN is irradiated under light, electrons are excited from

VB to CB in both CN and CIS. And, under the collective effect of IEF and the band bending assisted by the Coulomb interaction, the electrons in the CB of CN are transferred to the VB of CIS, where they neutralize with the holes of CIS (Fig. 8(c)). In this way, electrons in the CB of CIS and holes in the VB of CN remain and are freed with a high thermodynamic energy to realize efficient redox

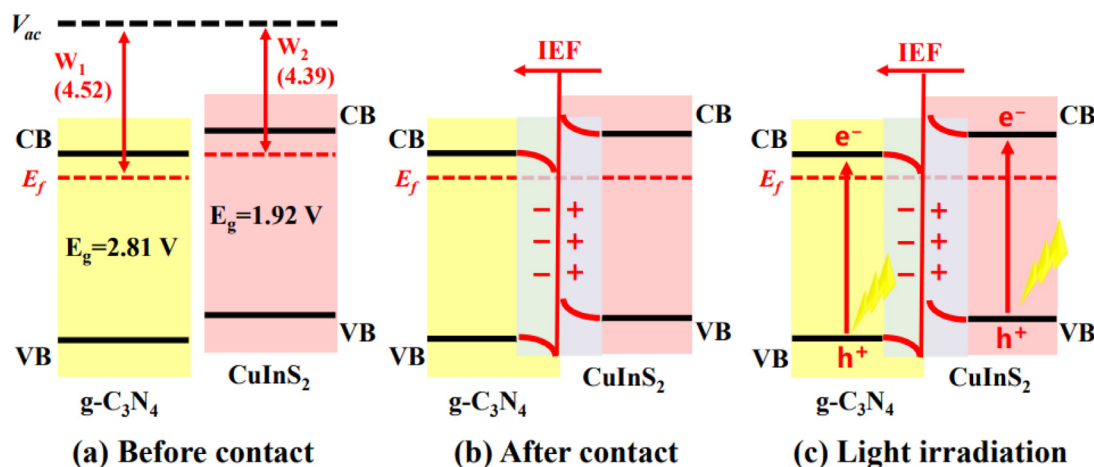


Fig. 8. S-scheme CN/CIS heterojunction: (a) before contact, (b) after contact and (c) after contact in light.

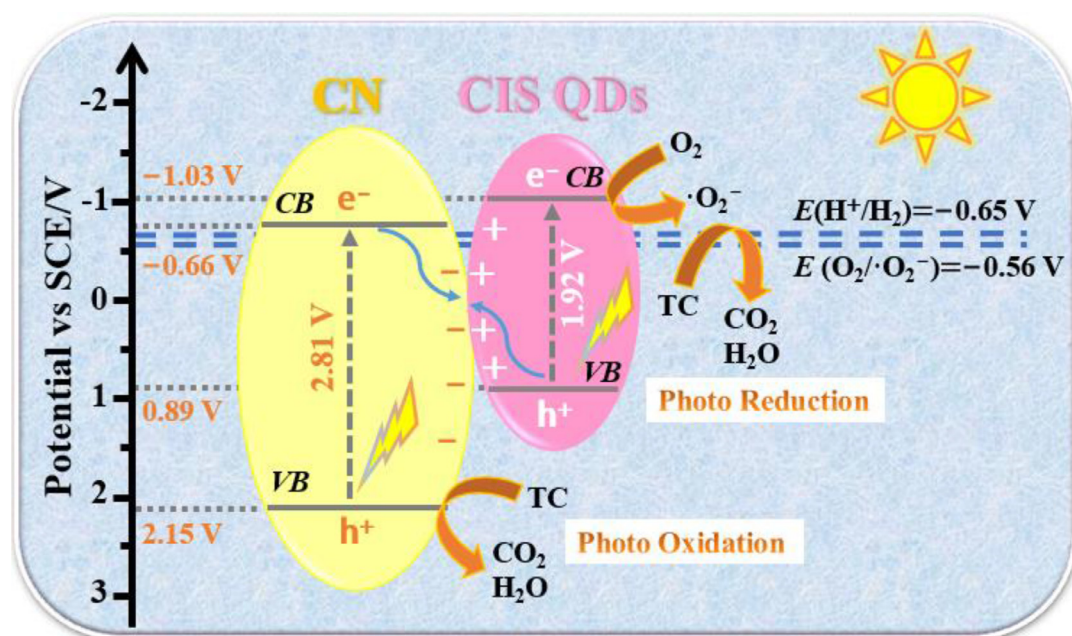


Fig. 9. Photocatalytic mechanism of the CIS/CN composites.

reactions for the generation of hydrogen or degradation of TC under stipulated conditions.

Based on our investigations, a possible redox pathway has been suggested and intended to highlight the charge generation and transfer in the prepared CIS/CN nanocomposites, as is depicted in Fig. 9. When CIS QDs and CN are in a close interaction, electrons in CIS QDs are naturally transferred via the interface to CN till the same Fermi energy level is accomplished in both sides. Since CIS QDs donate excited electrons, a positive charge is acquired while CN is gaining electrons and a negative charge at the interface is acquired. Thus, an IEF is accomplished at the interface, which is directed from CIS to CN. The established IEF facilitates the charge conductivity and the separation of the photogenerated charge carrier pairs. Meanwhile, the band edge of both CIS QDs and CN is respectively placed upwards attributed to the demise of electrons and downwards due to the gain of them. During the photocatalysis, through light treatment, the electrons of CIS QDs and CN are excited from their corresponding VBs to CBs, forming extra coulomb interaction. The altered IEF and the band bending associated with the coulomb interaction enforce the low-energy photoexcited electrons of CN to preferentially meet with the low-energy holes in the

VB of CIS QDs. Thus, a S-scheme interface is established for photo-generated charge transfer [55–57].

The S-scheme charge transfer mechanism is further explained on the basis of the band structure of the materials, as is presented in Fig. 4(d). In a S-scheme heterojunction route [58], the excited electrons in the CB of CIS entertain a potential of  $-1.03$  V (vs SCE) and possess enough thermodynamic energy to reduce  $O_2$  to produce  $\cdot O_2^-$  and  $H^+$  to  $H_2$ . Accordingly, this S-scheme effectively improves the charge separation while enhancing the photocatalytic activity for hydrogen generation and TC decomposition.

#### 4. Conclusion

CIS QDs were successfully prepared and combined with CN to construct CIS/CN nanocomposites as efficient photocatalysts for the production of hydrogen and the degradation of TC. With the composite materials, the photocatalytic oxidation of tetracycline and hydrogen evolution significantly increased. The degradation rate of 100 mL (40 mg/L) of TC solution with 10CIS/CN was 52.16% in 120 min, which was 3.4 times that of  $g-C_3N_4$ . With the same photocatalyst,  $102.4 \mu\text{mol g}^{-1} \text{h}^{-1}$  of hydrogen was produced in 1 h.

The high photocatalytic presentation of CIS/CN was mainly accredited to the development of S-scheme heterojunctions between CIS QDs and CN. The handy interaction amongst the CIS QDs and CN was conducive to transferring the photoexcited electrons from CN to CIS QDs. Therefore, electrons quickly participated in the photocatalytic process. This work is an effort to amend CN with polysulfide quantum dots and bargain a fresh idea for augmenting the performance of CN.

### Credit authorship contribution statement

Jingjing Zhang conducted catalysts synthesis, characterization and activity test. Yue Zhao contributed to data analysis and discussed the photocatalytic mechanism. Kezhen Qi and Shu-yuan Liu conceived the project and wrote the manuscript.

### Declaration of Competing Interest

The authors declare that they have no known competing financial interests or personal relationships that could have appeared to influence the work reported in this paper.

### Acknowledgements

This work was financially supported by [National Natural Science Foundation of China](#) (Nos. 52272287, 22268003 and 22202138). Project from Yunnan Province (Nos. 202301AT070027, 202305AF150116) and Development Fund from Dali University (No. KY2296129740).

### References

- [1] S. Tiba, A. Omri, *Renew. Sust. Energy Rev.* 69 (2017) 1129–1146.
- [2] H. Arminen, A.N. Menegaki, *Energy Econ.* 80 (2019) 621–634.
- [3] H. Mikulcic, X. Wang, N. Duic, R. Dewil, *J. Environ. Manage.* 259 (2020) 109666.
- [4] J. Zhang, X. Gu, Y. Zhao, K. Zhang, Y. Yan, K. Qi, *Nanomaterials* 13 (2023) 305.
- [5] L. Yuan, C. Han, M.-Q. Yang, Y.-J. Xu, *Int. Rev. Phys. Chem.* 35 (2016) 1–36.
- [6] F. He, A. Meng, B. Cheng, W. Ho, J. Yu, *Chin. J. Catal.* 41 (2020) 9–20.
- [7] G. Wang, Y. Quan, K. Yang, Z. Jin, *J. Mater. Sci. Technol.* 121 (2022) 28–39.
- [8] F. Xu, K. Meng, B. Cheng, S. Wang, J. Xu, J. Yu, *Nat. Commun.* 11 (2020) 4613.
- [9] Z. Wang, Y. Chen, L. Zhang, B. Cheng, J. Yu, J. Fan, *J. Mater. Sci. Technol.* 56 (2020) 143–150.
- [10] X. Li, Q. Luo, L. Han, F. Deng, Y. Yang, F. Dong, *J. Mater. Sci. Technol.* 114 (2022) 222–232.
- [11] B. Zhu, H. Tan, J. Fan, B. Cheng, J. Yu, W. Ho, *J. Materiomics* 7 (2021) 988–997.
- [12] X. Fei, H. Tan, B. Cheng, B. Zhu, L. Zhang, *Acta Phys.-Chim. Sin.* 37 (2021) 2010027.
- [13] S. Liu, K. Wang, M. Yang, Z. Jin, *Acta Phys.-Chim. Sin.* 38 (2022) 2109023.
- [14] L. Zhou, Y. Li, Y. Zhang, L. Qiu, Y. Xing, *Acta Phys.-Chim. Sin.* 38 (2022) 2112027.
- [15] J. Zhang, L. Zhang, W. Wang, J. Yu, *J. Phys. Chem. Lett.* 13 (2022) 8462–8469.
- [16] K. Qi, N. Cui, M. Zhang, Y. Ma, G. Wang, Z. Zhao, A. Khataee, *Chemosphere* 272 (2021) 129953.
- [17] K. Qi, S.-y. Liu, A. Zada, *J. Taiwan Inst. Chem. Eng.* 109 (2020) 111–123.
- [18] K. Qi, Y. Xie, R. Wang, S.-y. Liu, Z. Zhao, *Appl. Surf. Sci.* 466 (2019) 847–853.
- [19] Q. Xu, L. Zhang, B. Cheng, J. Fan, J. Yu, *Chem* 6 (2020) 1543–1559.
- [20] W. Shi, W. Sun, Y. Liu, X. Li, X. Lin, F. Guo, Y. Hong, *Renew. Energy* 182 (2022) 958–968.
- [21] B. Zhang, H. Shi, Y. Yan, C. Liu, X. Hu, E. Liu, J. Fan, *Colloid. Surface. A* 608 (2021) 125598.
- [22] C. Zhang, M. Jia, Z. Xu, W. Xiong, Z. Yang, J. Cao, H. Peng, H. Xu, Y. Xiang, Y. Jing, *Chem. Eng. J.* 430 (2022) 132652.
- [23] M. Sayed, B. Zhu, P. Kuang, X. Liu, B. Cheng, A.A.A. Ghamdi, S. Wageh, L. Zhang, J. Yu, *Adv. Sustain. Syst.* 6 (2022) 2100264.
- [24] J. Zhang, A. Bifulco, P. Amato, C. Imparato, K. Qi, *J. Colloid Interf. Sci.* 638 (2023) 193–219.
- [25] K. Qi, W. Lv, I. Khan, S.-y. Liu, *Chin. J. Catal.* 41 (2020) 114–121.
- [26] Z. Lu, C. Li, J. Han, L. Wang, S. Wang, L. Ni, Y. Wang, *Appl. Catal. B-Environ.* 237 (2018) 919–926.
- [27] H. Feng, Q. Guo, Y. Xu, T. Chen, Y. Zhou, Y. Wang, M. Wang, D. Shen, *ChemSusChem* 11 (2018) 4256–4261.
- [28] A. Boulesbaa, K. Wang, M. Mahjouri-Samani, M. Tian, A.A. Puzosky, I. Ivanov, C.M. Rouleau, K. Xiao, B.G. Sumpter, D.B. Geohegan, *J. Am. Chem. Soc.* 138 (2016) 14713–14719.
- [29] G. Wang, H. Wei, J. Shi, Y. Xu, H. Wu, Y. Luo, D. Li, Q. Meng, *Nano Energy* 35 (2017) 17–25.
- [30] Z. Long, W. Zhang, J. Tian, G. Chen, Y. Liu, R. Liu, *Inorg. Chem. Front.* 8 (2021) 880–897.
- [31] B. Liu, C. Bie, Y. Zhang, L. Wang, Y. Li, J. Yu, *Langmuir* 37 (2021) 14114–14124.
- [32] Y. Li, Y. Wang, R. Tang, X. Wang, P. Zhu, X. Zhao, C. Gao, *J. Phys. Chem. C* 119 (2015) 2963–2968.
- [33] Z. Zhu, X. Tang, C. Ma, M. Song, N. Gao, Y. Wang, P. Huo, Z. Lu, Y. Yan, *Appl. Surf. Sci.* 387 (2016) 366–374.
- [34] H.J. Kong, D.H. Won, J. Kim, S.I. Woo, *Chem. Mater.* 28 (2016) 1318–1324.
- [35] C. Liu, H. Huang, X. Du, T. Zhang, N. Tian, Y. Guo, Y. Zhang, *J. Phys. Chem. C* 119 (2015) 17156–17165.
- [36] G.J. Gomes, M.F. Zalazar, C.A. Lindino, F.R. Scremin, P.R.S. Bittencourt, M.B. Costa, N.M. Peruchena, *Micropor. Mesopor. Mater.* 252 (2017) 17–28.
- [37] C.-H. Tsai, D.K. Mishra, C.-Y. Su, J.-M. Ting, *Int. J. Energ. Res.* 38 (2014) 418–428.
- [38] S. Gu, X. Zhao, X. Zhou, F. Xie, X. Wang, Z. Tang, *ChemPlusChem* 85 (2020) 142–150.
- [39] C. Li, Z. Xi, W. Fang, M. Xing, J. Zhang, *J. Solid State Chem.* 226 (2015) 94–100.
- [40] Y. Yang, H. Zhang, Y. Zhao, Y. Song, H. Wu, S. Yang, *Diam. Relat. Mater.* 59 (2015) 13–20.
- [41] B. Bhattacharyya, A. Pandey, *J. Am. Chem. Soc.* 138 (2016) 10207–10213.
- [42] J. Wang, J. Chen, P. Wang, J. Hou, C. Wang, Y. Ao, *Appl. Catal. B-Environ.* 239 (2018) 578–585.
- [43] R.-R. Cui, X. Guo, X.-Y. Gong, C.-Y. Deng, *Rare Met.* 40 (2021) 2882–2891.
- [44] X. Li, K. Xie, L. Song, M. Zhao, Z. Zhang, *ACS Appl. Mater. Interfaces* 9 (2017) 24577–24583.
- [45] C. Xing, Z. Wu, D. Jiang, M. Chen, *J. Colloid Interf. Sci.* 433 (2014) 9–15.
- [46] H. Liyanaarachchi, C. Thambiliyagodage, C. Liyanaarachchi, U. Samarakoon, *Arab. J. Chem.* 16 (2023) 104749.
- [47] X. Wu, Y. Huang, Q. Bai, Q. Fan, G. Li, X. Fan, C. Zhang, H. Liu, *Mater. Sci. Semicon. Proc.* 37 (2015) 250–258.
- [48] X. Jia, J. Cao, H. Lin, M. Zhang, X. Guo, S. Chen, *Appl. Catal. B-Environ.* 204 (2017) 505–514.
- [49] R. Yu, B. Luo, M. Chen, D. Xu, X. Wu, D. Li, Y. Huang, Z. Xie, N. Shen, S. Meng, W. Shi, *Int. J. Hydrogen Energy* 48 (2023) 24285–24294.
- [50] M. Hojamberdiev, M.M. Khan, Z. Kadirova, K. Kawashima, K. Yubuta, K. Teshima, R. Riedel, M. Hasegawa, *Renew. Energy* 138 (2019) 434–444.
- [51] Z. Xu, J. Zhong, J. Chen, M. Li, L. Zeng, H. Yang, *Surf. Interfaces* 38 (2023) 102838.
- [52] M. Shao, Y. Shao, J. Chai, Y. Qu, M. Yang, Z. Wang, M. Yang, W.F. Ip, C.T. Kwok, X. Shi, Z. Lu, S. Wang, X. Wang, H. Pan, *J. Mater. Chem. A* 5 (2017) 16748–16756.
- [53] Y. Xiao, Z. Wang, L. Li, Q. Gu, M. Xu, L. Zhu, X. Fu, *Int. J. Hydrogen Energy* 48 (2023) 15460–15472.
- [54] Y. Li, Z. Xia, Q. Yang, L. Wang, Y. Xing, *J. Mater. Sci. Technol.* 125 (2022) 128–144.
- [55] L. Wang, C. Bie, J. Yu, *Trends Chem.* 4 (2022) 973–983.
- [56] C. Cheng, B. Zhu, B. Cheng, W. Macyk, L. Wang, J. Yu, *ACS Catal.* 13 (2023) 459–468.
- [57] L. Wang, B. Zhu, J. Zhang, J.B. Ghasemi, M. Mousavi, J. Yu, *Matter* 5 (2022) 4187–4211.
- [58] J. Fu, Q. Xu, J. Low, C. Jiang, J. Yu, *Appl. Catal. B-Environ.* 243 (2019) 556–565.